Nano Research

Open Access

Research Article

Mild photothermal therapy-enhanced nano-ferroptosis inducer for potent treatment of advanced prostate cancer

Xiao Hu[1,2,§], Fei Li[1,§], Xin-Hang Qian[1,§], Yu-Sen Zhang[1], Shuai Ke[1], Yun-Xia Jin[4], Shuai Yuan[1], Yuan-Yuan Zhang[1], Rui Li[5], Lei Cao[2], Lang Rao[2], Xian-Tao Zeng[1,3] ✉, and Ling-Ling Zhang[1] ✉

[1] *Center for Evidence-Based and Translational Medicine, Zhongnan Hospital of Wuhan University, Wuhan 430071, China*
[2] *Institute of Chemical Biology, Shenzhen Bay Laboratory, Shenzhen 518132, China*
[3] *Department of Urology, Zhongnan Hospital of Wuhan University, Wuhan 430071, China*
[4] *Hubei Collaborative Innovation Center for Advanced Organic Chemical Materials, Ministry of Education Key Laboratory for the Synthesis and Application of Organic Functional Molecules & College of Chemistry and Chemical Engineering, Hubei University, Wuhan 430062, China*
[5] *Xinjiang Key Laboratory of Solid State Physics and Devices, School of Physics Science and Technology, Xinjiang University, Urumqi 830017, China*
[§] *Xiao Hu, Fei Li, and Xin-Hang Qian contributed equally to this work.*

Cite this article: *Nano Research*, **2025**, *18*, 94907314. https://doi.org/10.26599/NR.2025.94907314

ABSTRACT: Androgen deprivation therapy (ADT) and androgen receptor signaling inhibitors (ARSis) often have limited efficacy in patients with advanced prostate cancer (PCa) (especially AR-negative). Inducing ferroptosis in PCa cells is an attractive therapeutic approach. In this work, mesoporous polydopamine nanoparticles (MPDA NPs) were developed to simultaneously deliver Cu^{+}/Cu^{2+} ion pairs and glutathione peroxidase 4 (GPX4) inhibitor RSL3 to tumor sites for enhanced treatment of PCa. The prepared MPDA-Cu-RSL3@HA (MPCRH) NPs induced ferroptosis by promoting lipid peroxidation and regulating phospholipid profiles in PCa cells, and the above effects were further enhanced by mild photothermal therapy (mPTT) without damaging normal tissues. mPTT can promote reactive oxygen species (ROS) generation and degrade tumor extracellular matrix *in vivo* to promote nanodrugs intratumoral penetration. In short, this work shows the great application potential of mPTT-enhanced nano-ferroptosis inducers in the field of PCa treatment, in order to provide a reasonable paradigm for nanodrug development and PCa treatment.

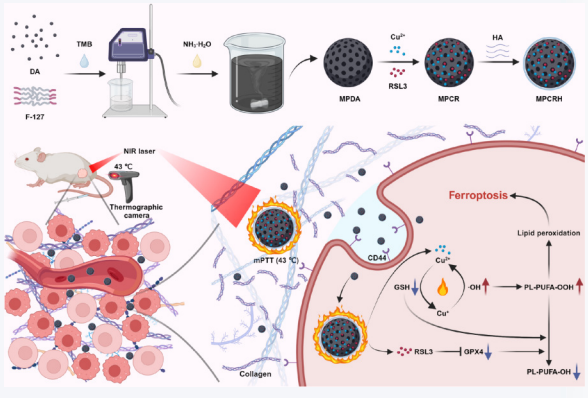

KEYWORDS: prostate cancer, ferroptosis, mild photothermal therapy, chemodynamic therapy, mesoporous polydopamine

1 Introduction

Prostate cancer (PCa) is one of the most common male malignancies. Among male cancer patients worldwide, the incidence (14.1%) and mortality (6.8%) of PCa rank second and fifth among all cancers, respectively [1, 2]. Although men with PCa initially respond to androgen deprivation therapy (ADT), unfortunately, nearly all patients who receive ADT eventually progress to the fatal stage of castration-resistant prostate cancer (CRPC) [3, 4]. And with the widespread use of new generation androgen receptor signaling inhibitors (ARSis) in the treatment of CRPC in recent years [5, 6], the proportion of drug-resistant phenotypes with loss of androgen receptor (AR) expression among CRPC patients, including neuroendocrine prostate cancer and double-negative prostate cancer, has increased significantly [7]. These patients will not benefit from ADT or ARSis and often have poor clinical outcomes. Therefore, it is urgent to develop a new therapy for PCa that does not rely on inhibiting AR signaling. Interestingly, studies showed that PCa cells lacking AR expression were highly sensitive to ferroptosis [8–10].

Ferroptosis is an iron-dependent form of programmed cell death driven by uncontrolled lipid peroxidation on cell membranes [11]. Since malignant tumor cells have greater metabolic pressure than normal cells, their iron uptake is significantly enhanced [12]. In

Received: December 16, 2024; **Revised:** February 13, 2025
Accepted: February 16, 2025

✉Address correspondence to Xian-Tao Zeng, zengxiantao1128@whu.edu.cn; Ling-Ling Zhang, llzhang@whu.edu.cn

addition, increased reactive oxygen species (ROS) production and abnormal lipid metabolism are often present in cancer cells [13]. All of the above factors will increase the sensitivity of cancer cells to ferroptosis. Proteomic data showed that the expression level of glutathione peroxidase 4 (GPX4) in PCa cell lines was much higher than that in benign prostate cell lines [14], whose main function is to reduce lethal phospholipid hydroperoxides (PL-OOHs) in membrane lipids to non-lethal phospholipid alcohols (PL-OHs) by catalyzing the reaction of glutathione (GSH) with lipid peroxides [15, 16]. RSL3 is a ferroptosis inducer (FIN) that can directly inhibit GPX4 activity [16]. However, as a small molecule compound, RSL3 has poor solubility, short blood half-life, and insufficient accumulation in tumor sites, which lead to weakened efficacy. In addition, it causes systemic toxicity due to nonspecific GPX4 inhibition. These characteristics severely limit its clinical application.

Nano drug delivery systems (NDDSs) have been widely used in preclinical studies of tumor treatment, among which mesoporous polydopamine nanoparticles (MPDA NPs) are an ideal NDDS with excellent biosafety and biodegradability, which can achieve efficient drug loading [17, 18]. In addition, the catechol structure of MPDA NPs makes it have a strong chelating effect on Cu^{2+} [19]. The low redox potential of Cu^{+}/Cu^{2+} (~ 0.16 V) makes it very easy for the two to convert into each other [20]. Cu^{2+} will be reduced to Cu^{+} by the excess GSH in cancer cells, and Cu^{+} can generate ROS by catalyzing Fenton-like reactions in the weakly acidic tumor microenvironment [21–23]. Therefore, copper-doped MPDA NPs (MPC NPs) can regulate the tumor redox level through Cu^{+}/Cu^{2+} ion pairs, generating ·OH while consuming GSH. At the same time, MPDA NPs have excellent photothermal conversion efficiency and can effectively increase the temperature of the tumor area under local near-infrared (NIR) laser irradiation, which can effectively accelerate the Fenton reaction rate [24, 25]. The dense and hard extracellular matrix (ECM) limits the penetration of drugs into tumor tissues, while mild photothermal therapy (mPTT) at around 43 °C can increase tumor vascular permeability and degrade the dense ECM without damaging normal tissues, thereby increasing drug delivery and penetration [26, 27].

This study constructed a nano-FIN enhanced by mPTT for the treatment of PCa, and used various prostate cancer cell lines and prostate cancer subcutaneous tumor mouse models for proof-of-concept studies. The specific idea is to synthesize MPDA NPs with a uniform mesoporous structure, then doped with copper and loaded with RSL3, and finally modify them with hyaluronic acid (HA) to ensure their physiological stability [28], namely MPDA-Cu-RSL3@HA (MPCRH) NPs. Theoretically, the nano-FIN can regulate the redox level of PCa and inhibit the self-ferroptosis resistance system of PCa, and its effect can be further enhanced by mPTT (Fig. 1).

2 Experimental

2.1 Preparation of MPCH, MPRH and MPCRH NPs

For MPDA-Cu-RSL3 (MPCR) NPs, the MPDA, $CuCl_2{\cdot}2H_2O$ and RSL3 were stirred in an ethanol solution at a mass ratio of 50:5:1. After 24 h, the precipitate was collected by centrifugation at 12,000 rpm for 10 min and washed three times with anhydrous ethanol. The supernatant of each step was collected for drug loading determination. The feed ratio and preparation method of MPDA-Cu (MPC) NPs and MPDA-RSL3 (MPR) NPs were the same as above. The PBS solutions (1 mg/mL) of MPDA, MPC, MPR and MPCR NPs were mixed with HA aqueous solution (2 mg/mL) respectively, stirred at room temperature for 24 h, and

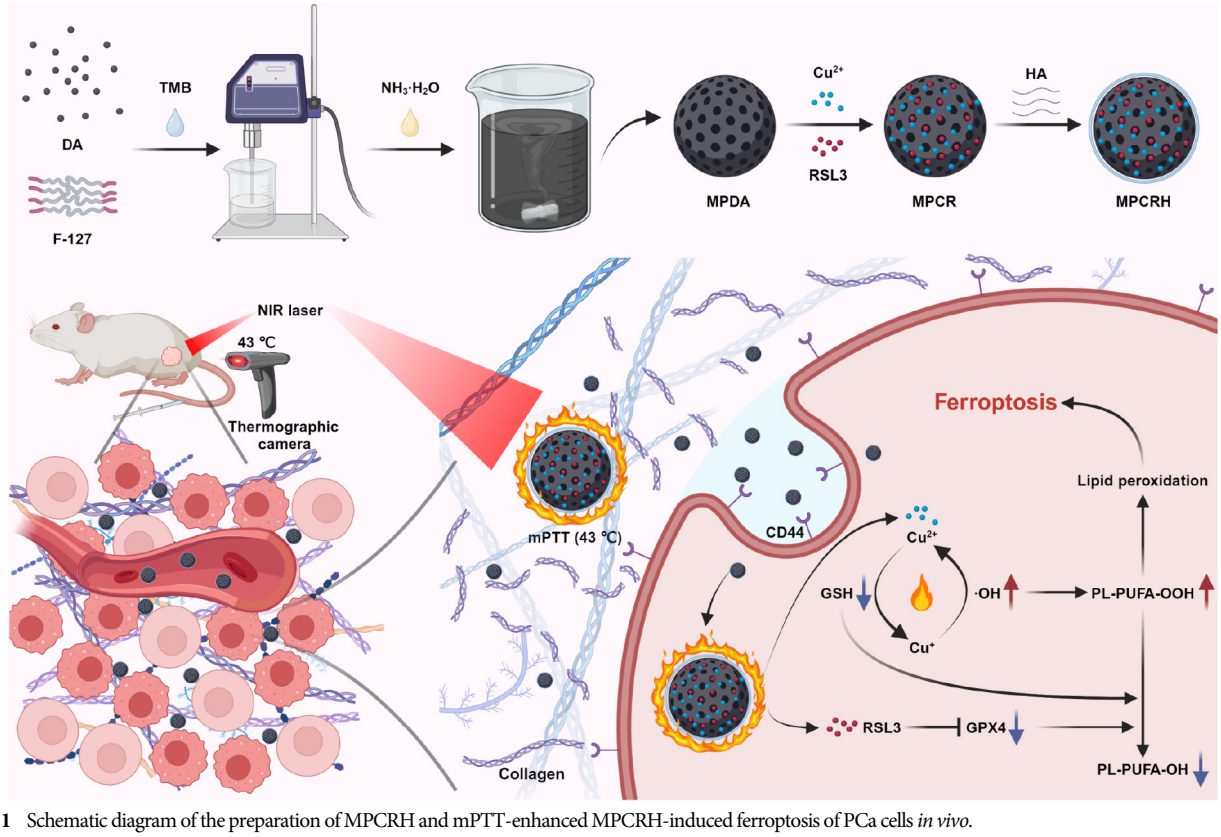

Figure 1 Schematic diagram of the preparation of MPCRH and mPTT-enhanced MPCRH-induced ferroptosis of PCa cells *in vivo*.

the precipitates were collected. After washing three times with PBS, MPH (MPDA@HA NPs), MPCH (MPC@HA NPs), MPRH (MPR@HA NPs), and MPCRH (MPCR@HA NPs) were obtained.

2.2 Cellular uptake assay

MPCRI (MPCR-ICG) and MPCRIH (MPCRI@HA) were prepared. Briefly, MPCR and indocyanine green (ICG) were mixed at a mass ratio of 1:1 and stirred. After 24 h, the precipitate was collected and washed three times with PBS. HA was modified as above.

DU145 or RM-1 cells were seeded into six-well plates at a density of 1×10^5 cells per well and incubated overnight. The corresponding nanodrugs were added and incubated for another 6 h. The final concentration of MPCRI or MPCRIH was 25 μg/mL, and the HA pretreatment group was pretreated with a medium containing 10 mg/mL HA for 2 h before adding MPCRIH. Hoechst 33258 staining solution was added and incubated for 20 min to mark the cell nucleus before observing the cells using a confocal laser scanning microscope (CLSM, Leica). Samples that needed to be analyzed by flow cytometry were digested and collected, and ICG fluorescence was detected using a Cyto-Flex flow cytometer (Beckman).

2.3 Cell viability assay

Cell viability was detected using the cell counting kit-8 (CCK-8) assay. In brief, DU145 or RM-1 was added to 96-well plates at a density of 5000 cells per well, and the corresponding nanodrugs were added after overnight incubation. The group that did not require NIR laser irradiation continued to incubate for 24 h. The group that required irradiation was irradiated 6 h after the addition of the nanodrugs (1 W/cm^2, 10 min) and continued to be cultured for 18 h. The absorbance at 450 nm of each well was detected by a microplate reader (Thermo Fisher) 3 h after the addition of CCK-8 working solution.

2.4 Cellular ROS, mitochondrial membrane potential and lipid peroxidation detection

DU145 or RM-1 cells were seeded into six-well plates at a density of 1×10^5 cells per well, and the corresponding nanodrugs were added after overnight incubation. NIR laser irradiation treatment is the same as 2.3. After different treatments, the medium containing 2',7'-dichlorodihydrofluorescein diacetate (DCFH-DA) probe was added, and the intracellular 2',7'-dichlorofluorescein (DCF) was directly observed using an inverted fluorescence microscope (IX71, OLYMPUS, Japan) or the cell suspension was collected and detected using a flow cytometer. In terms of mitochondrial membrane potential and lipid peroxidation detection, operation steps were similar except that 5,5',6,6'-tetrachloro-1,1',3,3'-tetraethylbenzimidazolylcarbocyanine iodide (JC-1) or 4,4-difluoro-5-((2-(4-(dimethylamino)phenyl)ethenyl)-3,5-dimethylphenyl)-4-bora-3a,4a-diaza-s-indacene (C11 BODIPY) probe instead of DCFH-DA was added.

2.5 Apoptosis detection

After different treatments, the cells were digested and collected in each group, and an additional group of untreated cells was prepared for two single-staining tubes for compensation adjustment. Cells in each group were added to 0.5 mL binding buffer for resuspending, and 5 μL Annexin V-FITC or 10 μL propidium iodide (PI) was added to each group, and the fluorescence of FITC and PI was detected on the flow cytometer after compensation adjustment.

2.6 Establishment of tumor models

All animal experimental protocols in this study have been approved by the Experimental Animal Ethics Committee of Zhongnan Hospital of Wuhan University (Permit No. ZN2024033) and were performed in accordance with the National Institutes of Health guide for the care and use of Laboratory animals. Specific pathogen free (SPF)-grade male C57BL/6 mice aged 4 to 6 weeks and weighing 18 to 22 g were selected as experimental animals.

RM-1 cell suspension containing 5×10^5 cells was injected subcutaneously into the right back of mice. The mice were then checked daily and their body weight and tumor volume were recorded. Tumor volume was measured using a vernier caliper and the calculation equation was as follows (Eq. (1)):

$$\text{Volume} = \frac{\text{Tumor long axis} \times \text{Tumor wide axis}^2}{2} \quad (1)$$

2.7 *In vivo* distribution of nanodrugs

Nine mice were selected to establish subcutaneous tumor models and randomly divided into MPCR group, MPCRH group, and MPCRH with laser (MPCRH + L) group. When the tumor volume reached 200 mm^3, nanodrugs were administered via tail vein. The mice were anesthetized with sodium pentobarbital at 3, 6, 12 and 24 h after administration, and the drug distribution was observed using an *in vivo* imaging system (IVIS). In the "MPCRH + L" group, the tumor area was irradiated with NIR laser (1 W/cm^2, 10 min) 30 min before each observation, and the temperature of the tumor area was monitored to maintain it at 43 ± 0.5 °C. After the last *in vivo* imaging, the mice were euthanized, and the heart, liver, spleen, lung, kidney and tumor were dissected for *ex vivo* imaging.

2.8 *In vivo* pharmacodynamic evaluation of mPTT-enhanced nano-FIN

25 mice were used to construct subcutaneous tumor models and randomly divided into 5 groups, namely, saline group, MPCH group, MPRH group, MPCRH group, and "MPCRH + L" group. Treatment began when the tumor volume reached 50 mm^3. The dose for each administration was 20 mg/kg. 12 h after each administration, the "MPCRH + L" group underwent mPTT for 10 min. Treatment was performed once every two days for a total of three treatments. Body weight and tumor volume were monitored, and monitoring ended on day 12 after the start of treatment. After anesthetizing the mice, whole blood and serum were collected. Then the mice were euthanized and samples of heart, liver, spleen, lung, kidney and tumor tissue were collected. The tumors were weighed and the tumor grow inhibition rate (TGI) was calculated as follows (Eq. (2)):

$$\text{TGI} = \frac{1 - \text{Tumor weight of the treatment group}}{\text{Tumor weight of the control group}} \times 100\% \quad (2)$$

Paraffin sections of tumors and major organs were prepared. Tumor sections were subjected to hematoxylin and eosin (H&E) staining, terminal deoxynucleotidyl transferase dUTP nick end labeling (TUNEL), Ki67 immunohistochemical staining, Masson staining, dihydroethidium (DHE) staining and GPX4 immunohistochemical staining.

The immunofluorescence and immunohistochemical staining image was semi-quantitatively analyzed as follows. First, the image was opened using ImageJ software. Then, it was converted to grayscale, and an appropriate threshold was applied to effectively distinguish the stained regions from the background. Depending on the analysis goal, either the number of positively stained cells or the area of the positive signal was quantified. Finally, the positive ratio was calculated by assessing the proportion of the stained area relative to the total area of interest.

H&E staining was performed on the tissue sections of the main organs. Whole blood samples were used to detect blood routine indicators. Serum samples were used to detect liver function indicators alanine aminotransferase (ALT) and aspartate aminotransferase (AST) as well as renal function indicators blood urea nitrogen (BUN) and creatinine (CRE).

2.9 Statistical analysis

All data were analyzed as the mean ± standard deviation obtained from at least three independent trials. The independent sample t test was used to compare two groups with a single influencing factor, the one-way ANOVA was used to compare multiple groups with a single influencing factor, and the two-way ANOVA was used to compare multiple groups with two influencing factors. Statistical values are indicated according to the following scale: $^{*}P < 0.05$, $^{**}P < 0.01$, $^{***}P < 0.001$, $^{****}P < 0.0001$, ns stands for not significant.

3 Results and discussion

3.1 Morphology and composition of MPCRH NPs

The specific synthesis steps of MPCRH NPs are shown in Fig. 2(a). The micromorphology of MPDA NPs was observed by SEM and TEM, showing that MPDA NPs were spherical particles with a uniform mesoporous structure and a particle size of about 350 nm (Fig. 2(b), and Fig. S1 in the Electronic Supplementary Material (ESM)), which facilitates subsequent drug loading (Fig. 2(b)), compared with polydopamine nanoparticles (PDA NPs) with no pores on the surface (Fig. S1 in the ESM). MPC NPs were prepared by chelating MPDA NPs with Cu^{2+} through catechol structure and HA was used to modify their surface to improve their stability and bioavailability. There was basically no change in morphology except for small particles formed partially on the surface due to Cu^{2+} chelation (Fig. 2(b)). After standing for 24 h, it was observed that

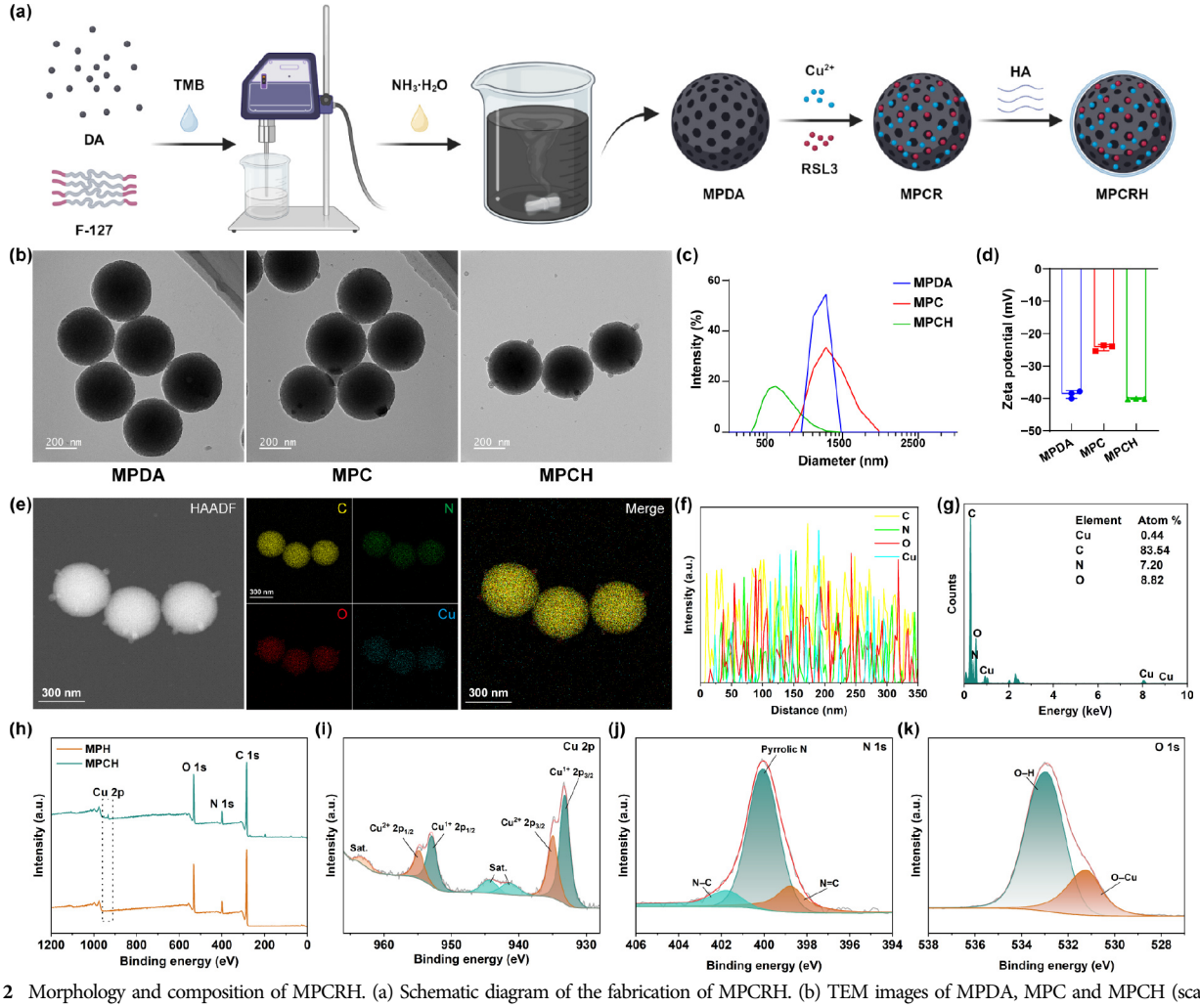

Figure 2 Morphology and composition of MPCRH. (a) Schematic diagram of the fabrication of MPCRH. (b) TEM images of MPDA, MPC and MPCH (scale bars: 200 nm). (c) Hydrodynamic sizes of MPDA, MPC and MPCH. (d) Zeta potentials of MPDA, MPC and MPCH. (e) HAADF-STEM image and corresponding elemental mapping images of MPCH (scale bars: 300 nm). (f) Co-localization of the distribution of elements in MPCH. (g) Semi-quantitative analysis of elements in MPCH by EDS. (h) XPS spectra of MPH and MPCH. High-resolution (i) Cu 2p, (j) N 1s and (k) O 1s XPS spectra of MPCH.

MPCH NPs were evenly distributed in the PBS solution while there were obvious aggregated precipitates in the MPC solution (Fig. S2(a) in the ESM). Furthermore, the long-term colloidal stability of MPCH NPs in different media (e.g., PBS, serum-containing medium) was observed (Fig. S2(b) in the ESM). The dynamic light scattering method was used to detect the hydrodynamic size and Zeta potential changes after each step of modification of MPDA NPs. After HA coating, the hydrodynamic diameter of MPCH NPs was significantly reduced to about 570 nm, and the polymer dispersity index (PDI) also decreased to 0.23 (Fig. 2(c), Table S1 in the ESM), demonstrating significantly improved dispersion of MPCH NPs. The hydrodynamic size of MPCH NPs was significantly larger than that observed in the dry state by transmission electron microscope (TEM), which may be due to the water absorption of HA itself [29], resulting in a thicker hydration layer of MPCH NPs in the solution environment. The change in Zeta potential also confirmed the gradual modification during the preparation of MPCH NPs (Fig. 2(d), Table S1 in the ESM).

The high-angle annular dark-field scanning transmission electron microscopy (HAADF-STEM) image and corresponding elemental mapping images showed that PDA-related carbon (C), nitrogen (N), oxygen (O), and metal element Cu were uniformly distributed on MPCH NPs (Figs. 2(e) and 2(f)). Semi-quantitative analysis of elements by energy dispersive spectrometer (EDS) showed that the Cu content of MPCH NPs was about 0.44% (Fig. 2(g)). X-ray photoelectron spectroscopy (XPS) was used to further analyze the oxidation state of Cu in MPCH NPs. The XPS spectrum of MPCH NPs had an additional Cu 2p peak compared to that of MPH NPs (Fig. 2(h)). In the high-resolution Cu 2p spectrum of MPCH NPs, Cu^{+} $2p_{3/2}$ peak (933.17 eV) and Cu^{+} $2p_{1/2}$ peak (952.86 eV) were consistent with the peak characteristics of Cu^{+} (Fig. 2(i)) [30]. Cu^{2+} $2p_{3/2}$ peak (934.95 eV), Cu^{2+} $2p_{1/2}$ peak (954.81 eV) and three Cu^{2+} satellite peaks proved the presence of Cu^{2+} (Fig. 2(i)) [19, 31], indicating the existence of Cu^{+}/Cu^{2+} ion pairs in MPCH NPs, which may be related to the strong reducing property of the catechol structure [32]. The ratio of Cu^{+} to Cu^{2+} was calculated to be 1.11 based on the peak area (Table S2 in the ESM), which is suitable for driving the redox cycle. High-resolution N 1s spectra showed that N in MPCH NPs was mainly present in the pyrrole five-membered ring structure formed by the self-polymerization of dopamine monomers (Fig. 2(j)). High-resolution O 1s spectra showed that most of O in MPCH NPs was present in the phenolic hydroxyl groups, and some participated in the formation of O–Cu coordination bonds (Fig. 2(k)).

3.2 Photothermal effect and redox activity of MPCRH NPs

It was detected that there was no significant difference in the loading content and encapsulation efficiency of RSL3 between the MPCR and MPR (Figs. 3(a) and 3(b), Fig. S3 in the ESM), which weren't affected by the coordination effect between MPDA NPs and Cu. The chemical structure similar to natural eumelanin gives MPDA a stable NIR photothermal conversion effect [24]. The temperature of the MPCH solution increased with the extension of NIR laser irradiation time, and its photothermal conversion effect was proportional to the MPCH concentration and laser power density (Figs. 3(c)–3(e)). In addition, the photothermal conversion effect of both MPH and MPCH didn't decay after three heating-cooling cycles (Fig. 3(f)). And Cu doping significantly enhanced the photothermal conversion efficiency (η) of MPH, which was 23.46% and 20.32% for MPCH and MPH, respectively (Fig. 3(g), Fig. S4 in the ESM).

Next, the redox activity of MPCH was further explored. In terms of GSH consumption, we found that MPCH significantly reduced the GSH content in the solution, which was proportional to the MPCH concentration and reaction time, while MPH had no similar effect (Figs. 3(h) and 3(i)). MPCH also had significant ·OH generation capacity compared to MPH (Fig. 3(j)), which was also proportional to the MPCH concentration and reaction time (Fig. 3(k)). MPCH generated ·OH through the Fenton-like reaction between Cu^{+} and H_2O_2, which was affected by the pH value, temperature and GSH concentration of the reaction environment (Fig. 3(m)). Therefore, we verified the impact of above factors on ·OH generation, and the results showed that changing the reaction environment from neutral to weakly acidic or adding GSH to the system can promote ·OH generation (Fig. 3(l)). It is worth mentioning that the tumor microenvironment is often slightly acidic and contains a large amount of GSH to resist the high-level ROS status [33]. In addition, the introduction of NIR laser to increase the local temperature can further promote the generation of ·OH (Fig. 3(l)).

3.3 Synergistic inhibitory effect of mPTT-enhanced MPCRH on PCa cells

We further explored the inhibitory effect of MPCRH on PCa cells. In order to clarify the uptake of MPCRH by PCa cells, ICG was used to label MPCRH to obtain MPCRIH. We found that the concentration of MPCRIH in DU145 cells increased with the extension of treatment time and reached a peak at 6 h (Fig. S5(a) in the ESM). Therefore, the optimal time point for laser irradiation after MPCRH treatment of PCa cells was clarified. HA can specifically bind to the CD44 receptor, which was found to be overexpressed on the surface of PCa cells [34, 35]. It was observed that compared with MPCRI-treated DU145 cells, the red fluorescence of MPCRIH-treated cells increased significantly, while the red fluorescence of MPCRIH in cells pretreated with HA was significantly reduced compared to the MPCRIH-treated group (Figs. 4(a) and 4(b), Fig. S5(b) in the ESM). Therefore, it can be proven that HA coating significantly promoted the uptake of nanodrugs by DU145 cells, which depended on the specific binding of HA to CD44 and the significant improvement in the solution stability of nanodrugs.

To verify the inhibitory effect of MPCRH on PCa, we selected human PCa cell lines including double-negative prostate cancer cell line DU145, neuroendocrine prostate cancer cell line PC-3, AR-positive CRPC cell line 22Rv1, AR-positive CSPC cell line LNCaP [36], and mouse AR-positive CRPC cell line RM-1 [37]. We also used human prostate hyperplasia cell line BPH-1 and human normal prostate epithelial cell line RWPE-1 as benign prostate cells. Regardless of whether combined with NIR laser, the inhibitory effect of MPCRH on PCa cells was significantly stronger than that on benign prostate cells, and it is worth mentioning that as the malignancy of the PCa cell line progressed, the inhibitory effect became stronger (Figs. 4(c) and 4(d), Table S3 in the ESM). It has been found that the more malignant AR-negative cells PC-3 and DU145 both express high levels of transferrin receptors, leading to increased iron uptake [8]. In addition, as the malignancy of PCa cell lines increases, expression of acyl-CoA synthetase long-chain family member 4 (ACSL4) in the cells also increases [10]. Researchers also found that AR signaling in PCa is associated with phospholipid

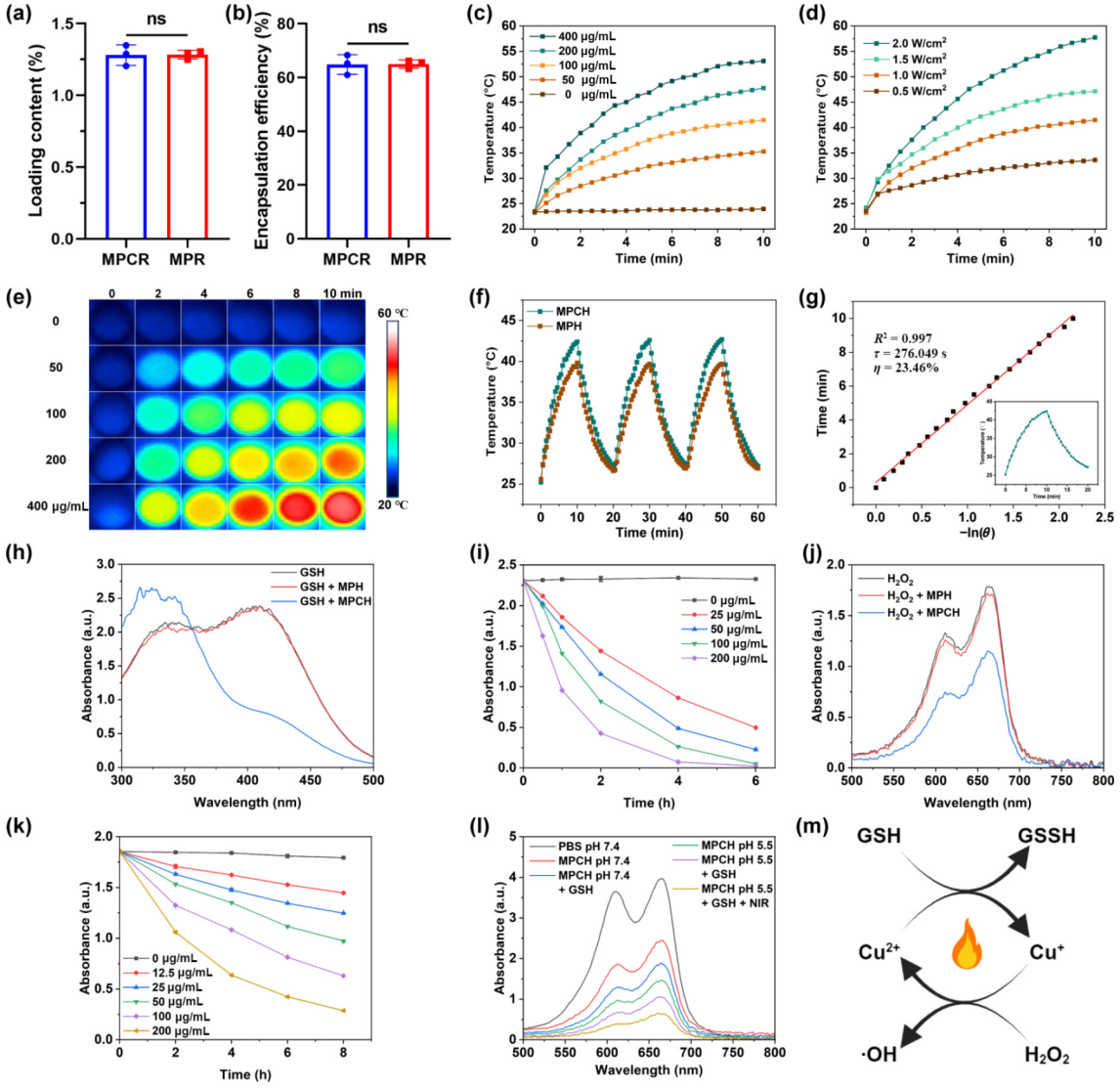

Figure 3 Photothermal effect and redox activity of MPCRH. (a) Loading content and (b) encapsulation efficiency of RSL3 in MPCR or MPR. (c) Temperature curves of MPCH solutions with different concentrations under NIR laser (1 W/cm²) irradiation. (d) Temperature curve of 100 μg/mL MPCH solution under NIR laser irradiation with different power densities. (e) Infrared thermal imaging images of MPCH solutions with different concentrations at different time points under NIR laser (1 W/cm²) irradiation. (f) Temperature curves of MPH solution and MPCH solution after three heating-cooling cycles (100 μg/mL, 1 W/cm²). (g) Photothermal conversion efficiency (η) calculated from cooling curves of MPCH solution (100 μg/mL, 1 W/cm²). (h) GSH consumption capacity of MPH and MPCH (100 μg/mL). (i) Concentration- and time-dependent GSH consumption capacity of MPCH. (j) ·OH generation capacity of MPH and MPCH (100 μg/mL). (k) Concentration- and time-dependent ·OH generation capacity of MPCH. (l) ·OH generation capacity of MPCH in different reaction environments (100 μg/mL). (m) Schematic diagram of the heating-enhanced Cu^+/Cu^{2+}-driven redox cycle.

remodeling, and AR-negative PCa cells were highly sensitive to ferroptosis [9]. In addition, we found that the introduction of NIR laser during low-concentration MPCRH treatment (< 100 μg) can selectively enhance its inhibitory effect on PCa cells without affecting its inhibitory effect on benign prostate cells (Fig. S6 in the ESM). This is because the mPTT below 43 °C mediated by MPCRH at a concentration below 100 μg/mL will not cause damage to normal cells, while the higher-temperature PTT mediated by MPCRH above 200 μg/mL will damage all cells including normal cells (Fig. 3(c)). Therefore, mPTT mediated by MPCRH can specifically enhance its inhibitory effect on PCa cells. Next, we explored the synergistic effect of each component in MPCRH. Both MPCH and MPRH can significantly inhibit PCa cells, and the inhibitory effect of MPCRH was further enhanced, regardless of whether combined with mPTT (Fig. 4(e)). In addition, RWPE-1 treated with MPRH showed a significant decrease in cell viability (Fig. 4(e)). In general, the mild toxicity of MPCRH to normal prostate cells is due to the nonspecific inhibition of GPX4 caused by the RSL3 loaded. The inhibitory effect of MPCRH on benign and malignant prostate cells can be rescued by the ferroptosis inhibitor Fer-1 (Fig. 4(e)), indicating that the effect of MPCRH was involved with ferroptosis. In short, the inhibition of MPCRH on PCa cells was enhanced by multiple advantages.

3.4 Synergistic pro-ferroptosis effect of mPTT-enhanced MPCRH

We further explored whether MPCRH induced ferroptosis by regulating redox homeostasis in PCa cells, leading to lipid peroxidation. DU145 and RM-1 were selected as PCa models for verification. It was found that the ROS content induced by MPCRH

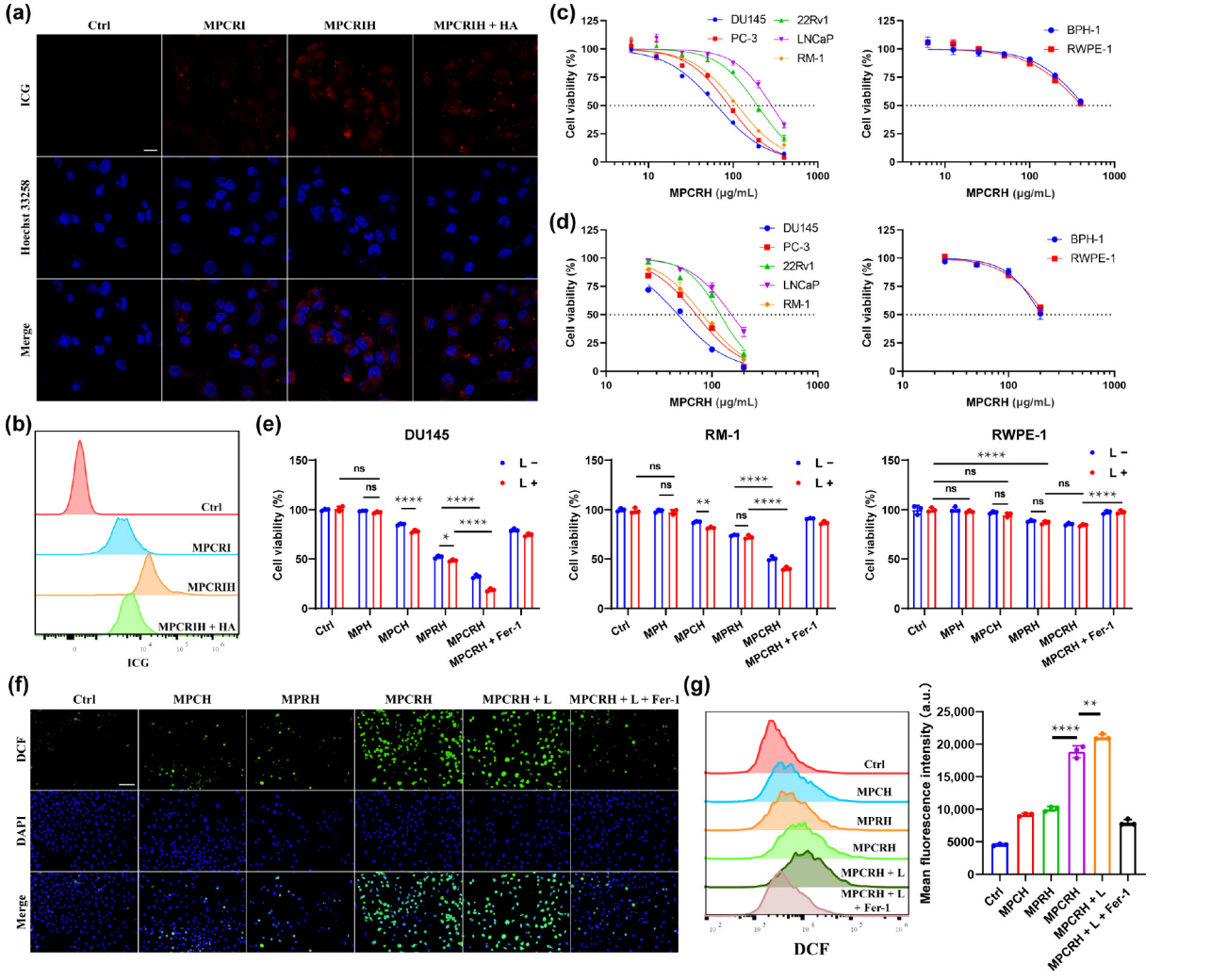

Figure 4 Synergistic inhibitory effect of mPTT-enhanced MPCRH on PCa cells. (a) CLSM images and (b) flow cytometry analysis of nanodrugs uptake by DU145 in each treatment group (nanodrugs: 25 μg/mL; HA: 10 mg/mL; scale bar: 20 μm). The inhibitory effects of MPCRH (c) without or (d) with NIR laser irradiation on PCa cells and benign prostate cells. (e) The inhibitory effects of nanodrugs containing different components on different cells (nanodrugs: 100 μg/mL; Fer-1: 2 μM). (f) Fluorescence microscopy images and (g) flow cytometry analysis of DCF in DU145 in each treatment group (nanodrugs: 50 μg/mL; Fer-1: 2 μM; scale bar: 100 μm).

in PCa cells was highest, which increased again after combining with mPTT (Figs. 4(f) and 4(g), Fig. S7 in the ESM). The addition of Fer-1 restored the intracellular ROS to the pre-treatment level (Figs. 4(f) and 4(g), Fig. S7 in the ESM). Mitochondria, as the core site of cellular oxidative metabolism, are the main source of ROS generation in cells [38]. Therefore, the excess ROS generated by MPCRH combined with mPTT may accumulate in mitochondria and ultimately causing mitochondrial damage. JC-1 aggregates in the matrix of healthy mitochondria to form multimers (red fluorescence) and exists as monomers in damaged mitochondria (green fluorescence). MPCRH could significantly increase the JC-1 monomers/aggregates ratio in PCa cells, indicating that it effectively induced mitochondrial oxidative damage, which was further aggravated after combined with mPTT (Fig. 5(a), Fig. S8 in the ESM). And Fer-1 can greatly inhibit the increase in JC-1 monomers induced by the combination treatment (Fig. 5(a), Fig. S8 in the ESM). The final occurrence of ferroptosis depends on the peroxidation of cell membrane lipids, which requires excessive ROS generation and final accumulation in membrane lipids. MPCRH, which can promote ROS generation and inhibit GPX4, significantly increased the lipid peroxidation level of PCa cells and can be further enhanced by combining mPTT (Figs. 5(b) and 5(c), Fig. S9 in the ESM). Fer-1 was also able to restore the lipid peroxidation to near normal levels (Figs. 5(b) and 5(c), Fig. S9 in the ESM). Each nanodrug can effectively induce apoptosis in cells, and MPCRH combined with mPTT had the strongest apoptosis-inducing effect (Figs. 5(d) and 5(e), Fig. S10 in the ESM). Similarly, Fer-1 can significantly restore the apoptosis-inducing effect of combined treatment (Figs. 5(d) and 5(e), Fig. S10 in the ESM).

3.5 Effect of mPTT-enhanced MPCRH on lipid metabolism in PCa cells

Considering the close connection between ferroptosis and lipid metabolism, we next explored the effect of mPTT-enhanced MPCRH on lipid metabolism in PCa cells. The groups were compared pairwise to screen out differential lipids. Among the 1027 lipids detected, some differential lipids were screened out in the comparison between each group (Fig. 6(a)). KEGG pathway enrichment analysis of differential lipids revealed that the ferroptosis pathway and the unsaturated fatty acid biosynthesis pathway, which is closely related to ferroptosis, were among the most enriched pathways in the comparison between the treatment

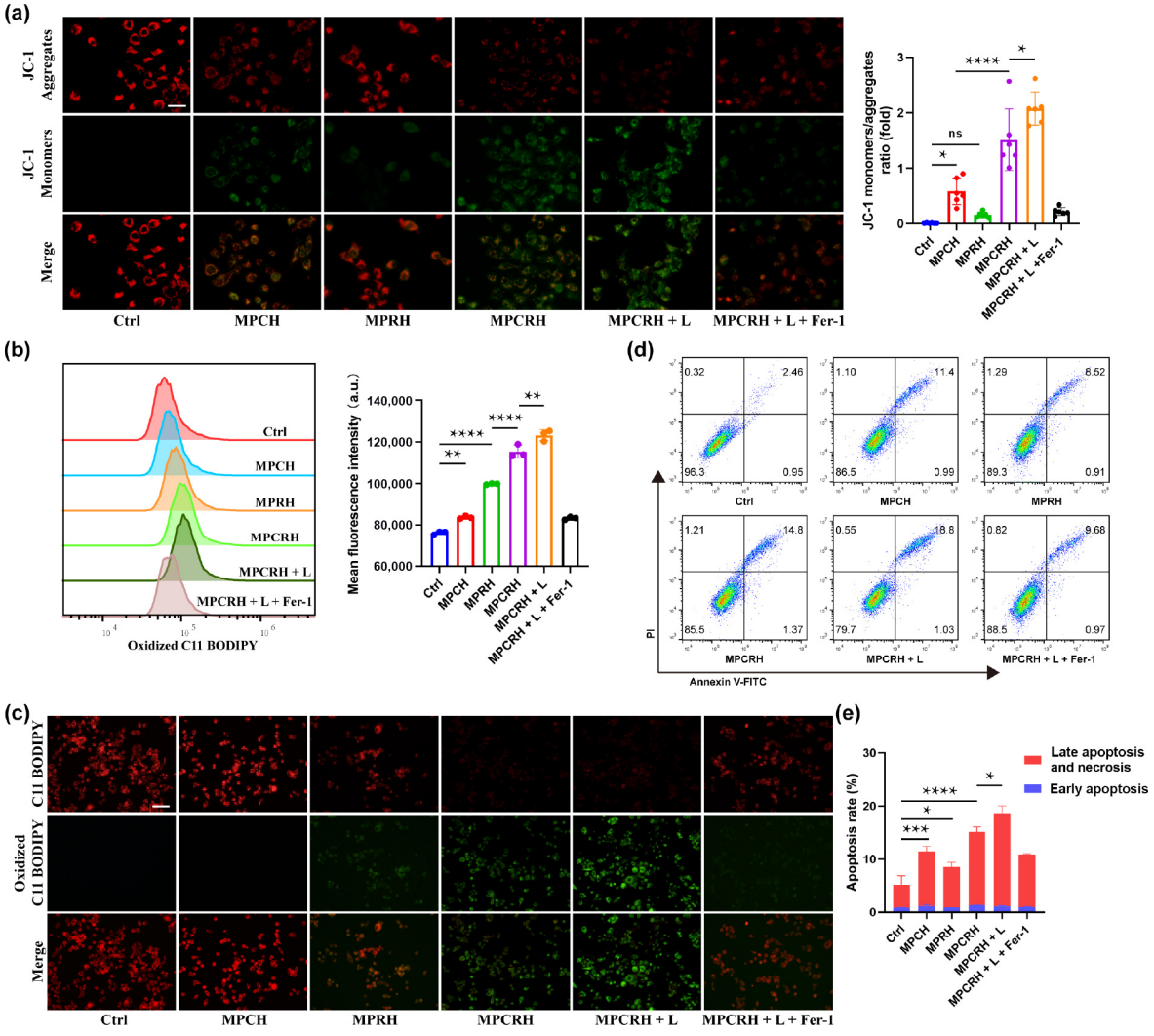

Figure 5 Synergistic pro-ferroptosis effect of mPTT-enhanced MPCRH. (a) Fluorescence microscopy images of JC-1 in DU145 in each treatment group and quantitative statistical results of the corresponding JC-1 monomers/aggregates ratio (scale bar: 50 μm). (b) Flow cytometry analysis and (c) fluorescence microscopy images of C11 BODIPY in DU145 in each treatment group (scale bar: 100 μm). (d) and (e) Flow cytometry analysis of MPCRH-induced apoptosis in DU145 (nanodrugs: 50 μg/mL; Fer-1: 2 μM).

group and the control group (Fig. 6(b)). In the comparison between the "MPCRH + L" group and the MPCH group, the ferroptosis pathway was also enriched. Furthermore, arachidonic acid (AA) and linoleic acid metabolism pathways were enriched, which are among the most susceptible polyunsaturated fatty acids (PUFAs) to be peroxidized (Fig. 6(b)) [39, 40]. The specific differences between the groups in the lipids annotated as ferroptosis-related in the Kyoto encyclopedia of genes and genomes (KEGG) database were further analyzed. In the comparison between treatment group and control group, three ferroptosis-related lipids were detected, two of which were significantly increased, namely AA (C20:4) and adrenoic acid (AdA) (C22:4), two PUFAs (Table S4 in the ESM). It has been reported that among all PUFA-containing PLs, phosphatidylethanolamines (PEs) containing AA or AdA tails are a more critical lipid signal driving ferroptosis [39]. Oxidized CoQ_{10} was increased in the comparison between "MPCRH + L" group and MPCH group (Table S4 in the ESM), which is an important antioxidant for cells to resist ferroptosis [41]. The significant increase in oxidized CoQ_{10} in the "MPCRH + L" group confirmed its more powerful ferroptosis-inducing effect. Since PL-PUFA (PL containing PUFA tails) is the preferred substrate for PL peroxidation and studies have found that MUFA can inhibit ferroptosis by competitively replacing PUFA tails in membrane PLs [42], the contents of each PL in three groups were statistically analyzed based on the differential PL spectra containing unsaturated fatty acid tails between "MPCRH + L" group and control group (Fig. 6(c)). It was found that all PL-MUFAs showed a downward trend in the "MPCRH + L" group (Fig. 6(d)), and the content of PL-O-PUFAs (ether phospholipids with PUFA tails) showed a characteristic increase (Fig. 6(e)). It has been reported that extensive downregulation of PL-O-PUFAs, which served as substrates for lipid peroxidation, can transform cancer cells that were initially sensitive to ferroptosis into a ferroptosis-resistant state in mice [43]. The PL profile characteristics of PCa cells in the "MPCRH + L" group, with low PL-MUFAs and high PL-O-PUFAs, suggested that this treatment enhanced the ferroptosis-sensitive state of PCa cells.

3.6 Targeting and efficacy of mPTT-enhanced MPCRH against PCa *in vivo*

Inspired by the excellent effect of MPCRH *in vitro*, we explored the

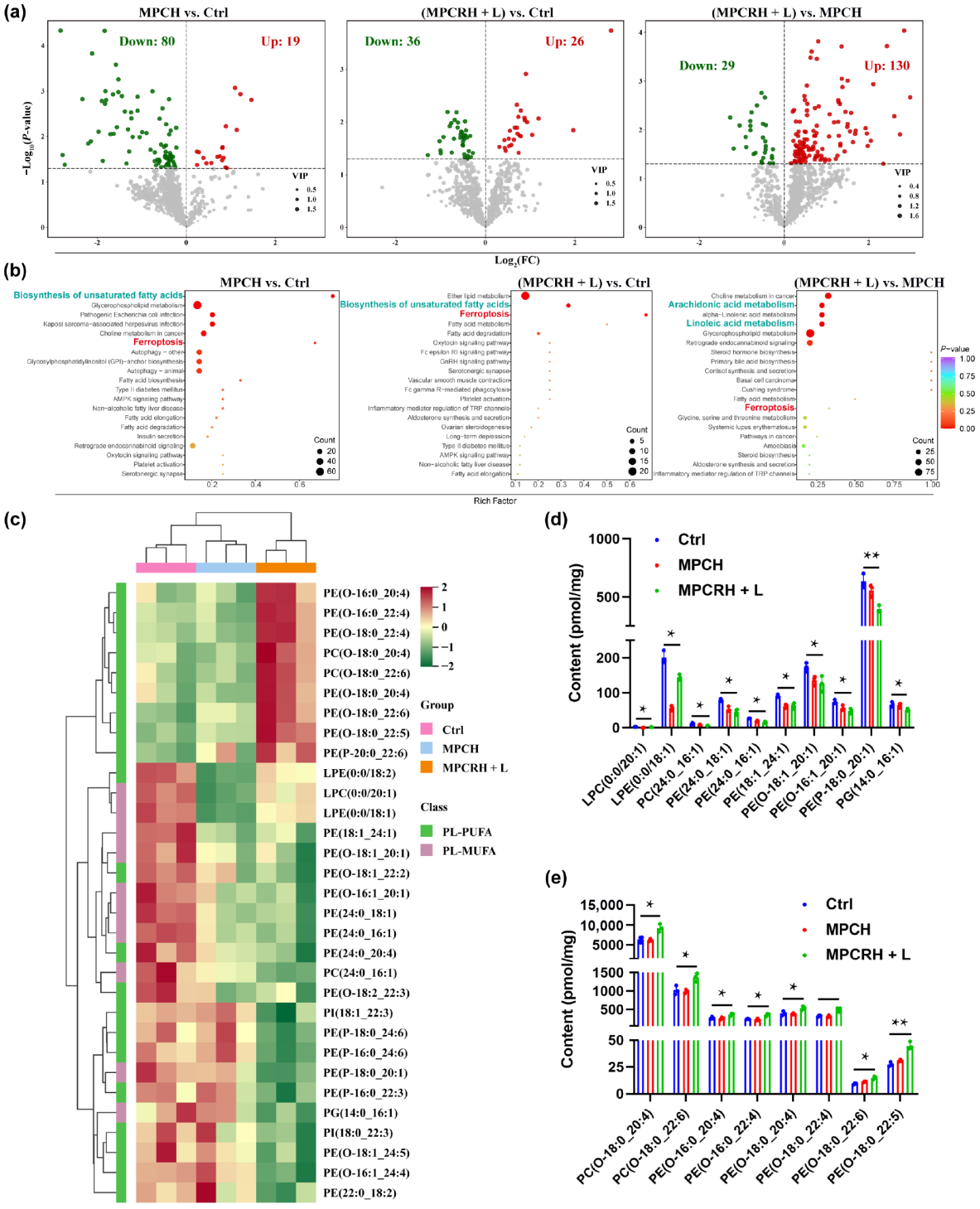

Figure 6 Effect of mPTT-enhanced MPCRH on lipid metabolism in PCa cells. (a) Results of differential lipid screening among treatment groups in DU145. (b) KEGG pathway enrichment analysis results of differential lipids among treatment groups. (c) Heat map of the contents of PL-PUFAs and PL-MUFAs in the differential PL profiles of each treatment group and (d) the specific contents of differential PL-MUFAs and (e) differential PL-O-PUFAs in each group.

targeting of MPCRH to PCa *in vivo*. Prior to animal experiments, MPCRH was confirmed to have good blood biocompatibility through hemolysis tests (Fig. S11 in the ESM). Modification of HA on the surface of MPCR significantly enhanced its targeting to PCa (Figs. 7(a)–7(d)), which can be attributed to the prolonged blood circulation time and the specific binding of HA to CD44 receptor [34]. Combined with mPTT, the tumor targeting of MPCRH was further enhanced (Figs. 7(a)–7(d)), which may be because local mPTT at the tumor site was conducive to increasing tumor vascular permeability and destroying the dense ECM, thereby promoting the penetration of nanodrugs into tumor tissue [27, 44]. In addition, it was found that the concentration of MPCRH in the tumor site reached a peak 12 h after intravenous injection (Figs. 7(a) and 7(c)), thus determining the optimal time point for performing mPTT in mice. 24 h after intravenous injection, the mice were euthanized and tumor tissues and organs were collected for *in vitro* imaging. It

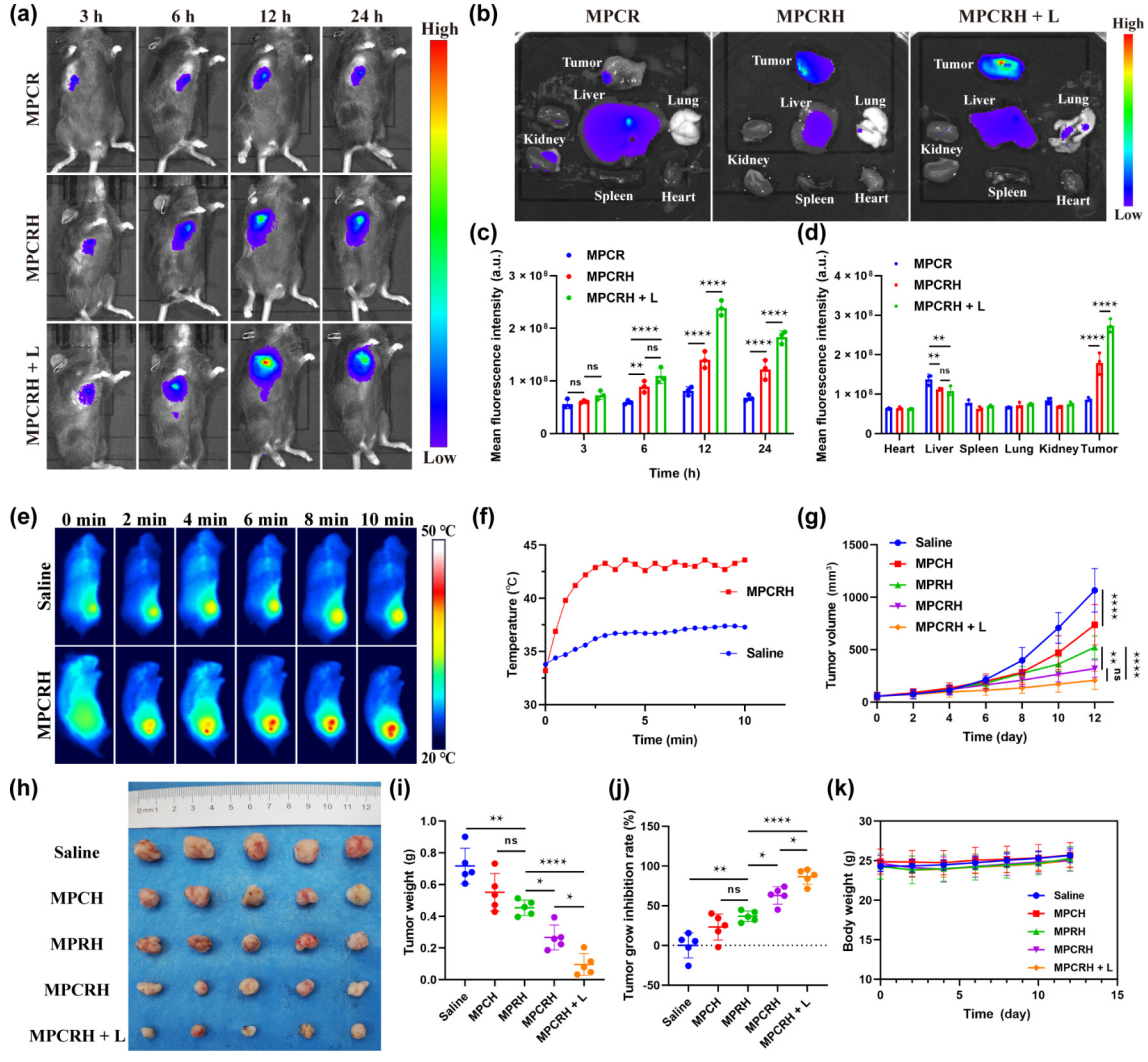

Figure 7 Targeting and efficacy of mPTT-enhanced MPCRH against PCa *in vivo*. (a) IVIS fluorescence images of mice in each group at different time points and (c) the mean fluorescence intensity of the tumor site. (b, d) Distribution of nanodrugs in various organs of mice 24 h after intravenous injection. (e) Thermal imaging images of mice treated with mPTT 12 h after injection of saline or MPCRH and (f) the temperature curves of the corresponding tumor area. (g) Tumor growth curves of mice in each group during treatment. (h) Images of tumor tissue dissected from mice after treatment. (i) Tumor weight and (j) corresponding tumor grow inhibition rate of mice in each group after treatment. (k) Body weight changes of mice in each group.

was observed that most of the MPCR accumulated in liver, a small part in tumor and kidney, while MPCRH mainly accumulated in tumor, with a small part in liver (Figs. 7(b) and 7(d)). Combined with mPTT, the accumulation of MPCRH in tumor further increased (Figs. 7(b) and 7(d)). Therefore, we speculated that local mPTT in the tumor area can promote the penetration of nanodrugs that were originally blocked around the tumor by destroying the fibrotic ECM.

Mice were subjected to mPTT 12 h after drug injection. Under NIR laser irradiation, MPCRH were able to raise the temperature of the tumor area to about 43 °C within 3 min, and then intermittent irradiation was performed to maintain the temperature at 43 ± 0.5 °C, which lasted for 10 min (Figs. 7(e) and 7(f)). In contrast, the tumor temperature of mice injected with saline was still below 37.5 °C even after 10 min of irradiation (Figs. 7(e) and 7(f)). The entire course of treatment for the mouse PCa model is shown in Fig. S12 in the ESM. The statistical results of tumor volume growth curve showed that the tumor inhibitory effect of MPCRH was further enhanced compared to MPRH, while there was no significant difference between "MPCRH + L" group and MPCRH group (Figs. 7(g) and 7(h), Fig. S13 in the ESM). The statistical results of tumor weight and tumor inhibition rate after treatment showed similar effects, and mPTT significantly improved the tumor inhibition rate of MPCRH (Figs. 7(i) and 7(j)). It was shown that the mPTT-enhanced nano-FIN we prepared did not cause significant systemic toxicity by monitoring the weight changes of mice during treatment and detecting blood routine and blood biochemical indicators after treatment (Fig. 7(k), Figs. S14 and S15 in the ESM). H&E staining of major organ tissue sections showed that each group showed typical normal tissue morphology (Fig. S16 in the ESM).

3.7 *In vivo* therapeutic mechanism of mPTT-enhanced MPCRH

H&E staining results of tumor tissue sections showed obvious changes in tumor cell morphology in MRCRH and "MPCRH + L" groups, with cell nuclei condensed and fragmented, concentrated cytoplasm, and increased cell necrosis area, while cell morphology

in other treatment groups was relatively intact (Fig. 8(a)). Through TUNEL staining, it can be seen that apoptotic cells in MRCRH and "MPCRH + L" groups were significantly more than those in other groups, which were further increased after combined with mPTT (Figs. 8(a) and 8(c)). The proliferative activity of tumor cells was evaluated through Ki67 staining. It can be observed that the expression of Ki67 in tumor cells was significantly reduced in MPCRH group, and the Ki67-positive rate of "MPCRH + L" group was the lowest (Figs. 8(a) and 8(d)). The collagen fibers in tumor tissue were labeled by Masson staining (blue area refers to collagen fiber) to quantify the ECM outside the tumor, which significantly reduced only in "MPCRH + L" group, and there was no difference in other treatment groups without mPTT (Figs. 8(a) and 8(e)). It was confirmed that mPTT can degrade the tumor ECM. Regarding ROS in tumors, MPCRH combined with mPTT induced the most ROS generation (Figs. 8(b) and 8(f)). In terms of GPX4 expression in tumor tissues, it was shown that "MPCRH + L" group had the lowest GPX4 expression, showing significant ferroptosis induction ability (Figs. 8(b) and 8(g)). In general, mPTT exerted two synergistic effects, including destruction of tumor ECM via collagen degradation and synergizing with the Cu^{+}/Cu^{2+} redox cycle to amplify ROS generation.

4 Conclusions

In summary, the mesoporous nanoparticles loaded with ferroptosis inducers and Cu^{+}/Cu^{2+} ion pairs constructed by us showed unique tumor specificity, efficient redox regulation ability and excellent ferroptosis-induced effect in multiple characteristic cell lines, and the anti-cancer ability was further enhanced by mPTT without damaging normal cells. In addition, in the CRPC transplanted tumor mouse model, the nanodrugs had significant PCa targeting and could degrade the dense ECM through local mPTT to promote intratumoral penetration of MPCRH, further demonstrating excellent *in vivo* synergistic therapeutic effects. It is hoped that this study can provide a reasonable paradigm for the treatment of CRPC, which is very intractable in clinical practice. Overall, mPTT-enhanced MPCRH has an advantage over other nanoplatforms in this field by emphasizing its dual Cu^{+}/Cu^{2+} redox system, mPTT-enhanced targeting and redox catalytic capabilities [23, 25]. On the other hand, this study still has some shortcomings, including the lack of long-term toxicity evaluation *in vivo* and the need for further optimization of drug release kinetics. In addition, we hope to explore PCa-specific targets in following work and further confirm the relevant genes and proteins that play a role in nanodrug-induced ferroptosis of PCa cells, in order to design nanodrugs with stronger specificity and higher efficacy for the treatment of CRPC.

Electronic Supplementary Material: Supplementary material (further details of experimental methods, SEM and TEM images, long-term colloidal stability, standard curve of RSL3, photothermal conversion efficiency of MPH, results of MPCRIH uptake by DU145 over time, inhibitory effects of MPCRH with NIR, *in vitro* experimental results of RM-1 cells, biocompatibility, experimental process and results of mPTT-enhanced MPCRH treatment *in vivo*) is available in the online version of this article at https://doi.org/10.26599/NR.2025.94907314.

Data availability

All data needed to support the conclusions in the paper are presented in the manuscript and the Electronic Supplementary Material. Additional data related to this paper may be requested from the corresponding author upon request.

Acknowledgements

This work was supported by the National Natural Science Foundation of China (Nos. 12204358 and 62204214), the Young Top-notch Talent Cultivation Program of Hubei Province (X.-T. Z.), the Fundamental Research Funds for the Central Universities

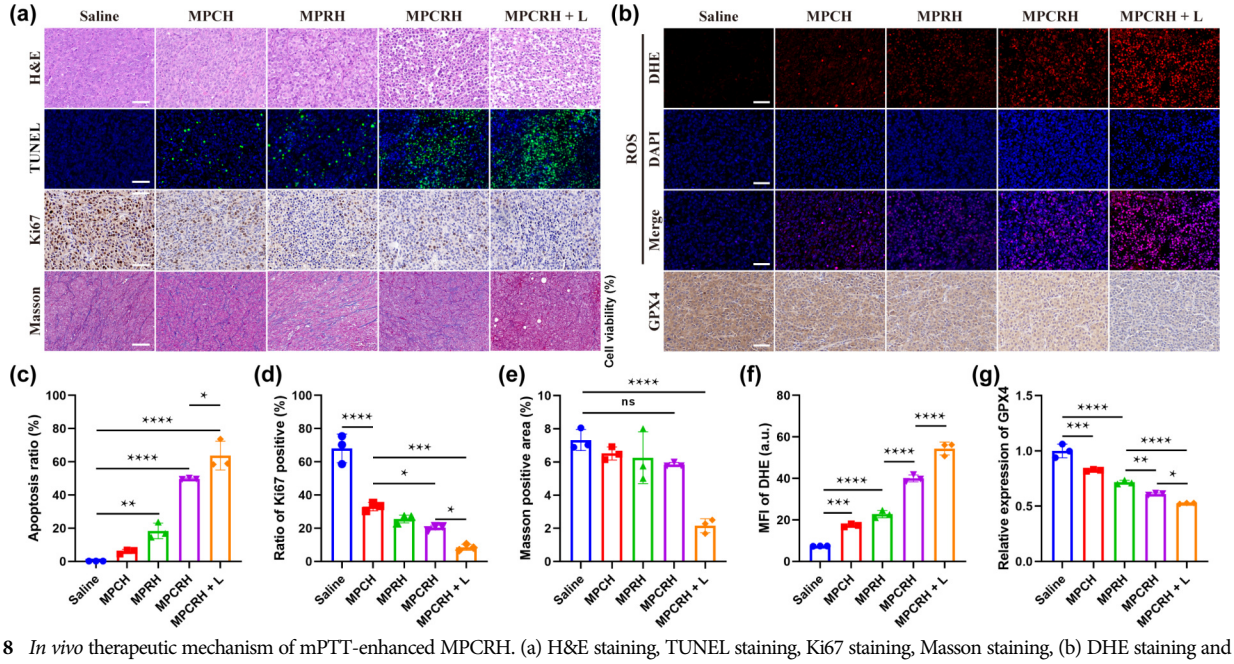

Figure 8 *In vivo* therapeutic mechanism of mPTT-enhanced MPCRH. (a) H&E staining, TUNEL staining, Ki67 staining, Masson staining, (b) DHE staining and GPX4 staining images of tumor tissue sections in each group. Scale bar in the Masson staining image is 100 μm, and the rest are 50 μm. Corresponding semi-quantitative analysis of (c) TUNEL staining, (d) Ki67 staining, (e) Masson staining, (f) DHE staining and (g) GPX4 staining ($n = 3$).

(No. 2042023kf0091), and the Youth Interdisciplinary Special Fund of Zhongnan Hospital of Wuhan University (No. ZNQNJC2022005).

Declaration of competing interest

All the contributing authors report no conflict of interests in this work.

Author contribution statement

X. H.: Investigation, methodology, writing – original draft, data curation, formal analysis, validation. F. L.: Data curation, formal analysis, validation. X.-H. Q.: Data curation, formal analysis, validation. Y.-S. Z.: Data curation, formal analysis, validation. S. K.: Data curation, formal analysis. Y.-X. J.: Data curation, formal analysis. S. Y.: Resources, data curation. Y.-Y. Z.: Formal analysis, funding. R. L.: methodology, resources, funding. L. C.: Methodology, writing – review & edition. L. R.: Methodology, writing – review & edition, resources. X.-T. Z.: Conceptualization, writing – review & edition, resources, funding. L.-L. Z.: Conceptualization, writing – review & edition, resources, funding. All the authors have approved the final manuscript.

Informed consent

Not applicable.

Ethics statement

All animal experimental protocols in this study have been approved by the Experimental Animal Ethics Committee of Zhongnan Hospital of Wuhan University (permit No. ZN2024033) and were performed in accordance with the National Institutes of Health guide for the care and use of Laboratory animals.

Use of AI statement

None.

References

[1] Sung, H.; Ferlay, J.; Siegel, R. L.; Laversanne, M.; Soerjomataram, I.; Jemal, A.; Bray, F. Global cancer statistics 2020: GLOBOCAN estimates of incidence and mortality worldwide for 36 cancers in 185 countries. *CA Cancer J. Clin.* **2021**, *71*, 209–249.

[2] Zi, H.; Liu, M. Y.; Luo, L. S.; Huang, Q.; Luo, P. C.; Luan, H. H.; Huang, J.; Wang, D. Q.; Wang, Y. B.; Zhang, Y. Y. et al. Global burden of benign prostatic hyperplasia, urinary tract infections, urolithiasis, bladder cancer, kidney cancer, and prostate cancer from 1990 to 2021. *Mil. Med. Res.* **2024**, *11*, 64.

[3] Ryan, C. J.; Smith, M. R.; de Bono, J. S.; Molina, A.; Logothetis, C. J.; de Souza, P.; Fizazi, K.; Mainwaring, P.; Piulats, J. M.; Ng, S. et al. Abiraterone in metastatic prostate cancer without previous chemotherapy. *N. Engl. J. Med.* **2013**, *368*, 138–148.

[4] Scher, H. I.; Fizazi, K.; Saad, F.; Taplin, M. E.; Sternberg, C. N.; Miller, K.; de Wit, R.; Mulders, P.; Chi, K. N.; Shore, N. D. et al. Increased survival with enzalutamide in prostate cancer after chemotherapy. *N. Engl. J. Med.* **2012**, *367*, 1187–1197.

[5] Alabi, B. R.; Liu, S. Q.; Stoyanova, T. Current and emerging therapies for neuroendocrine prostate cancer. *Pharmacol. Ther.* **2022**, *238*, 108255.

[6] Wang, W. L.; Epstein, J. I. Small cell carcinoma of the prostate: A morphologic and immunohistochemical study of 95 cases. *Am. J. Surg. Pathol.* **2008**, *32*, 65–71.

[7] Bluemn, E. G.; Coleman, I. M.; Lucas, J. M.; Coleman, R. T.; Hernandez-Lopez, S.; Tharakan, R.; Bianchi-Frias, D.; Dumpit, R. F.; Kaipainen, A.; Corella, A. N. et al. Androgen receptor pathway-independent prostate cancer is sustained through FGF signaling. *Cancer Cell* **2017**, *32*, 474–489.e6.

[8] Keer, H. N.; Kozlowski, J. M.; Tsai, Y. C.; Lee, C.; McEwan, R. N.; Grayhack, J. T. Elevated transferrin receptor content in human prostate cancer cell lines assessed *in vitro* and *in vivo*. *J. Urol.* **1990**, *143*, 381–385.

[9] Liang, D. G.; Feng, Y.; Zandkarimi, F.; Wang, H.; Zhang, Z. D.; Kim, J.; Cai, Y. Y.; Gu, W.; Stockwell, B. R.; Jiang, X. J. Ferroptosis surveillance independent of GPX4 and differentially regulated by sex hormones. *Cell* **2023**, *186*, 2748–2764.e22.

[10] Wang, M. E.; Chen, J. Q.; Lu, Y.; Bawcom, A. R.; Wu, J. J.; Ou, J. H.; Asara, J. M.; Armstrong, A. J.; Wang, Q. B.; Li, L. et al. *RB1*-deficient prostate tumor growth and metastasis are vulnerable to ferroptosis induction via the E2F/ACSL4 axis. *J. Clin. Invest.* **2023**, *133*, e166647.

[11] Stockwell, B. R. Ferroptosis turns 10: Emerging mechanisms, physiological functions, and therapeutic applications. *Cell* **2022**, *185*, 2401–2421.

[12] Rodriguez, R.; Schreiber, S. L.; Conrad, M. Persister cancer cells: Iron addiction and vulnerability to ferroptosis. *Mol. Cell* **2022**, *82*, 728–740.

[13] Viswanathan, V. S.; Ryan, M. J.; Dhruv, H. D.; Gill, S.; Eichhoff, O. M.; Seashore-Ludlow, B.; Kaffenberger, S. D.; Eaton, J. K.; Shimada, K.; Aguirre, A. J. et al. Dependency of a therapy-resistant state of cancer cells on a lipid peroxidase pathway. *Nature* **2017**, *547*, 453–457.

[14] Nusinow, D. P.; Szpyt, J.; Ghandi, M.; Rose, C. M.; McDonald, E. R.; Kalocsay, M.; Jané-Valbuena, J.; Gelfand, E.; Schweppe, D. K.; Jedrychowski, M. et al. Quantitative proteomics of the cancer cell line encyclopedia. *Cell* **2020**, *180*, 387–402.e16.

[15] Zhang, X. L.; Zhang, X.; Chen, S. T.; Liu, Y. X.; Cao, C.; Cheng, G. H.; Wang, S. Glutathione-depleting polyprodrug nanoparticle for enhanced photodynamic therapy and cascaded locoregional chemotherapy. *J. Colloid Interface Sci.* **2024**, *670*, 279–287.

[16] Yang, W. S.; SriRamaratnam, R.; Welsch, M. E.; Shimada, K.; Skouta, R.; Viswanathan, V. S.; Cheah, J. H.; Clemons, P. A.; Shamji, A. F.; Clish, C. B. et al. Regulation of ferroptotic cancer cell death by GPX4. *Cell* **2014**, *156*, 317–331.

[17] Guo, H. Y.; Wang, L. T.; Wu, W.; Guo, M. K.; Yang, L. K.; Zhang, Z. H.; Cao, L.; Pu, F. F.; Huang, X.; Shao, Z. W. Engineered biomimetic nanoreactor for synergistic photodynamic-chemotherapy against hypoxic tumor. *J. Controlled Release* **2022**, *351*, 151–163.

[18] Chen, F.; Xing, Y. X.; Wang, Z. Q.; Zheng, X. Y.; Zhang, J. X.; Cai, K. Y. Nanoscale polydopamine (PDA) Meets π–π interactions: An interface-directed coassembly approach for mesoporous nanoparticles. *Langmuir* **2016**, *32*, 12119–12128.

[19] Wang, Q. H.; Li, X. L.; Mao, J. Y.; Qin, X.; Yang, S. B.; Hao, J. N.; Guan, M. J.; Cao, Y. Y.; Li, Y. S. Biomimic binding affinity gradients triggered GSH-response of core-shell nanoparticles for cascade chemo/chemodynamic therapy. *Adv. Healthcare Mater.* **2022**, *11*, 2101634.

[20] Anandan, S.; Miyauchi, M. Ce-doped ZnO ($Ce_xZn_{1-x}O$) becomes an efficient visible-light-sensitive photocatalyst by co-catalyst (Cu^{2+}) grafting. *Phys. Chem. Chem. Phys.* **2011**, *13*, 14937–14945.

[21] Hu, W.; Yang, L. L.; Liao, H. T.; Sun, D. G.; Ouyang, X. K.; Wang, N.; Yang, G. C. Disulfiram-loaded CuO_2 nanocarriers for enhanced synergistic chemodynamic chemotherapy. *J. Colloid Interface Sci.* **2024**, *674*, 9–18.

[22] Ma, B. J.; Wang, S.; Liu, F.; Zhang, S.; Duan, J. Z.; Li, Z.; Kong, Y.; Sang, Y. H.; Liu, H.; Bu, W. B. et al. Self-assembled copper-amino

acid nanoparticles for *in situ* glutathione "AND" H_2O_2 sequentially triggered chemodynamic therapy. *J. Am. Chem. Soc.* **2019**, *141*, 849–857.

[23] Zhang, Y. Q.; Zhang, N.; Xing, J. H.; Sun, Y. W.; Jin, X.; Shen, C. L.; Cheng, L.; Wang, Y. Y.; Wang, X. W. *In situ* hydrogel based on Cu–Fe_3O_4 nanoclusters exploits oxidative stress and the ferroptosis/cuproptosis pathway for chemodynamic therapy. *Biomaterials* **2024**, *311*, 122675

[24] Liu, Y. L.; Ai, K. L.; Liu, J. H.; Deng, M.; He, Y. Y.; Lu, L. H. Dopamine-melanin colloidal nanospheres: An efficient near-infrared photothermal therapeutic agent for *in vivo* cancer therapy. *Adv. Mater.* **2013**, *25*, 1353–1359.

[25] Liu, D. D.; Dai, X. L.; Zhang, W.; Zhu, X. Y.; Zha, Z.; Qian, H. S.; Cheng, L.; Wang, X. W. Liquid exfoliation of ultrasmall zirconium carbide nanodots as a noninflammatory photothermal agent in the treatment of glioma. *Biomaterials* **2023**, *292*, 121917.

[26] Yu, X.; Liu, J. Y.; Bauer, A.; Wei, X. Q.; Smith, S.; Ning, S. P.; Wang, C. Z. Enhancing tumor endothelial permeability using MUC18-targeted gold nanorods and mild hyperthermia. *J. Colloid Interface Sci.* **2024**, *676*, 101–109.

[27] Xiong, Y. X.; Wang, W.; Deng, Q. Y.; Zhang, Z. J.; Wang, Q.; Yong, Z. T.; Sun, C. Y.; Yang, X. L.; Li, Z. F. Mild photothermal therapy boosts nanomedicine antitumor efficacy by disrupting DNA damage repair pathways and modulating tumor mechanics. *Nano Today* **2023**, *49*, 101767.

[28] Valachová, K.; Hassan, M. E.; Šoltés, L. Hyaluronan: Sources, structure, features and applications. *Molecules* **2024**, *29*, 739.

[29] Pérez, L. A.; Hernández, R.; Alonso, J. M.; Pérez-González, R.; Sáez-Martínez, V. Hyaluronic acid hydrogels crosslinked in physiological conditions: Synthesis and biomedical applications. *Biomedicines* **2021**, *9*, 1113.

[30] Jia, X. F.; Li, J.; Wang, E. K. Cu Nanoclusters with aggregation induced emission enhancement. *Small* **2013**, *9*, 3873–3879.

[31] Zhou, J.; Yu, Q.; Song, J.; Li, S.; Li, X. L.; Kang, B.; Chen, H. Y.; Xu, J. J. Photothermally triggered copper payload release for cuproptosis-promoted cancer synergistic therapy. *Angew. Chem., Int. Ed.* **2023**, *62*, e202213922.

[32] Perron, N. R.; Brumaghim, J. L. A review of the antioxidant mechanisms of polyphenol compounds related to iron binding. *Cell Biochem. Biophys.* **2009**, *53*, 75–100.

[33] Chao, Y.; Liu, Z. Biomaterials tools to modulate the tumour microenvironment in immunotherapy. *Nat. Rev. Bioeng.* **2023**, *1*, 125–138.

[34] Benitez, A.; Yates, T. J.; Lopez, L. E.; Cerwinka, W. H.; Bakkar, A.; Lokeshwar, V. B. Targeting hyaluronidase for cancer therapy: Antitumor activity of sulfated hyaluronic acid in prostate cancer cells. *Cancer Res.* **2011**, *71*, 4085–4095.

[35] Tan, H. S.; Liu, Y. L.; Hou, N.; Cui, S. S.; Liu, B.; Fan, S. S.; Yu, G. P.; Han, C.; Zheng, D. C.; Li, W. Z. et al. Tumor microenvironment pH-responsive pentagonal gold prism-based nanoplatform for multimodal imaging and combined therapy of castration-resistant prostate cancer. *Acta Biomater.* **2022**, *141*, 408–417.

[36] Ghoochani, A.; Hsu, E. C.; Aslan, M.; Rice, M. A.; Nguyen, H. M.; Brooks, J. D.; Corey, E.; Paulmurugan, R.; Stoyanova, T. Ferroptosis inducers are a novel therapeutic approach for advanced prostate cancer. *Cancer Res.* **2021**, *81*, 1583–1594.

[37] Zhong, W. B.; Wu, K. H.; Long, Z. N.; Zhou, X. M.; Zhong, C. F.; Wang, S.; Lai, H. H.; Guo, Y. F.; Lv, D. J.; Lu, J. M. et al. Gut dysbiosis promotes prostate cancer progression and docetaxel resistance via activating NF-κB-IL6-STAT3 axis. *Microbiome* **2022**, *10*, 94.

[38] Zeng, Z. S.; Luo, Y.; Xu, X. Y.; Shan, T.; Chen, M. X.; Huang, Z. Q.; Huang, Y. J.; Zhao, C. S. A mitochondria-targeting ROS-activated nanoprodrug for self-augmented antitumor oxidation therapy. *J. Controlled Release* **2023**, *359*, 415–427.

[39] Kagan, V. E.; Mao, G. W.; Qu, F.; Angeli, J. P. F.; Doll, S.; Croix, C. S.; Dar, H. H.; Liu, B.; Tyurin, V. A.; Ritov, V. B. et al. Oxidized arachidonic and adrenic PEs navigate cells to ferroptosis. *Nat. Chem. Biol.* **2017**, *13*, 81–90.

[40] Yang, W. S.; Kim, K. J.; Gaschler, M. M.; Patel, M.; Shchepinov, M. S.; Stockwell, B. R. Peroxidation of polyunsaturated fatty acids by lipoxygenases drives ferroptosis. *Proc. Natl. Acad. Sci. USA* **2016**, *113*, E4966–E4975.

[41] Bersuker, K.; Hendricks, J. M.; Li, Z. P.; Magtanong, L.; Ford, B.; Tang, P. H.; Roberts, M. A.; Tong, B. Q.; Maimone, T. J.; Zoncu, R. et al. The CoQ oxidoreductase FSP1 acts parallel to GPX4 to inhibit ferroptosis. *Nature* **2019**, *575*, 688–692.

[42] Magtanong, L.; Ko, P. J.; To, M.; Cao, J. Y.; Forcina, G. C.; Tarangelo, A.; Ward, C. C.; Cho, K.; Patti, G. J.; Nomura, D. K. et al. Exogenous monounsaturated fatty acids promote a ferroptosis-resistant cell state. *Cell Chem. Biol.* **2019**, *26*, 420–432.e9.

[43] Zou, Y. L.; Henry, W. S.; Ricq, E. L.; Graham, E. T.; Phadnis, V. V.; Maretich, P.; Paradkar, S.; Boehnke, N.; Deik, A. A.; Reinhardt, F. et al. Plasticity of ether lipids promotes ferroptosis susceptibility and evasion. *Nature* **2020**, *585*, 603–608.

[44] Kong, G.; Braun, R. D.; Dewhirst, M. W. Characterization of the effect of hyperthermia on nanoparticle extravasation from tumor vasculature. *Cancer Res.* **2001**, *61*, 3027–3032.